CrossMark

Poroelastic analysis of interstitial fluid flow in a single lamellar trabecula subjected to cyclic loading

Yoshitaka Kameo[1,2] · **Yoshihiro Ootao**[2] · **Masayuki Ishihara**[2]

Abstract Trabecula, an anatomical unit of the cancellous bone, is a porous material that consists of a lamellar bone matrix and interstitial fluid in a lacuno-canalicular porosity. The flow of interstitial fluid caused by deformation of the bone matrix is believed to initiate a mechanical response in osteocytes for bone remodeling. In order to clarify the effect of the lamellar structure of the bone matrix—i.e., variations in material properties—on the fluid flow stimuli to osteocytes embedded in trabeculae, we investigated the mechanical behavior of an individual trabecula subjected to cyclic loading based on poroelasticity. We focused on variations in the trabecular permeability and developed an analytical solution containing both transient and steady-state responses for interstitial fluid pressure in a single trabecular model represented by a multilayered two-dimensional poroelastic slab. Based on the obtained solution, we calculated the pressure and seepage velocity of the interstitial fluid in lacuno-canalicular porosity, within the single trabecula, under various permeability distributions. Poroelastic analysis showed that a heterogeneous distribution of permeability produces remarkable variations in the fluid pressure and seepage velocity in the cross section of the individual trabecula, and suggests that fluid flow stimuli to osteocytes are mostly governed by the value of permeability in the neighborhood of the trabecular surfaces if there is no difference in the average permeability in a single trabecula.

1 Introduction

Trabeculae are microstructural components of cancellous bone that maintain a three-dimensional network structure based on the applied mechanical loading. The arrangement of the trabeculae is continually reorganized owing to bone remodeling to satisfy mechanical demands. Figure 1 shows the schematic of the hierarchical bone structure from the cellular level to the organ level. Bone tissue is renewed by osteoclastic bone resorption and osteoblastic bone formation on individual trabecular surfaces, which is called the remodeling cycle (Parfitt 1994). Although the well-ordered cellular behavior during the process of the remodeling cycle is still unclear, osteocytes buried in calcified bone matrix are believed to be responsible for regulating the activities of osteoclasts and osteoblasts (Tatsumi et al. 2007; Bonewald 2011; Nakashima et al. 2011). From an anatomical point of view, the osteocyte network via slender cell processes housed in a lacuno-canalicular porosity is considered to be suitable for sensing the surrounding mechanical environment (Cowin et al. 1991; Sugawara et al. 2005; Himeno-Ando et al. 2012).

Experimental and theoretical studies have shown that the flow of interstitial fluid in a lacuno-canalicular porosity is likely to be a mechanical cue initiating an osteocytic response (Weinbaum et al. 1994; Burger and Klein-Nulend 1999; Price et al. 2011; Kameo and Adachi 2014). The interstitial fluid flow is triggered by deformation of the bone matrix under external loading, which is typically cyclic because of loco-

✉ Yoshitaka Kameo
  kameo@frontier.kyoto-u.ac.jp

[1] Department of Biomechanics, Research Center for Nano Medical Engineering, Institute for Frontier Medical Sciences, Kyoto University, 53 Kawahara-cho, Shogoin, Sakyo-ku, Kyoto 606-8507, Japan

[2] Department of Mechanical Engineering, Graduate School of Engineering, Osaka Prefecture University, 1-1 Gakuen-cho, Naka-ku, Sakai-shi, Osaka 599-8531, Japan
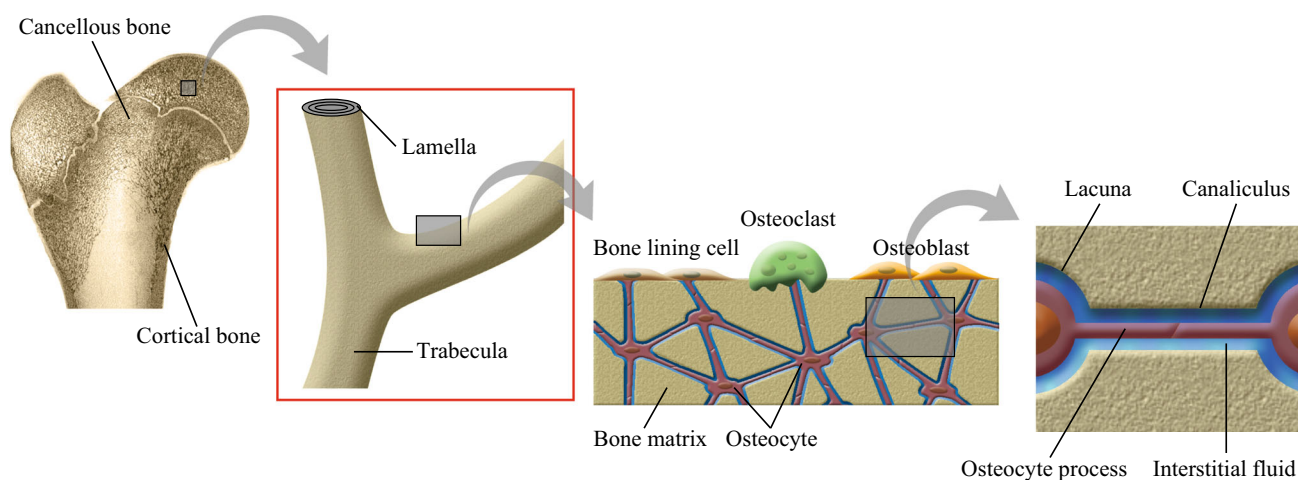
Fig. 1 Hierarchical bone structure from the cellular to the organ level. The individual trabeculae in cancellous bone contain a lamellar bone matrix and interstitial fluid in a lacuno-canalicular porosity

motion and the maintenance of posture (Weinbaum et al. 1994). As shown in Fig. 1, the bone matrix of trabeculae has a lamellar structure comprising mineral crystals and collagen fibers (Martin et al. 1998), formed by repeated remodeling cycles. Thus, the mechanical properties of the bone matrix are directional and different for each lamella. Indeed, the dispersion in the measured values of the bone material properties (e.g., Turner et al. 1999) suggests that these properties can vary spatially even in the same bone tissue. Among the various material properties, the heterogeneous distribution of permeability, which measures the ability of a porous material to transmit fluid, can significantly influence the behavior of interstitial fluid in the lacuno-canalicular porosity within the individual trabeculae (Beno et al. 2006; Kameo et al. 2010; Pereira and Shefelbine 2014).

For quantitative evaluation of the interstitial fluid flow in bone tissue, Biot's poroelastic theory (Biot 1941, 1955) has been widely used (Cowin 1999). Poroelasticity is a continuum theory that considers the mechanical behavior of fluid-saturated porous media based on the interaction between the deformation of the solid matrix and the flow of the internal fluid. A number of analytical studies on fluid-saturated bones have employed the poroelastic approach that considers bone tissue as an isotropic material (Zhang and Cowin 1994; Zeng et al. 1994) or a transversely isotropic material (Rémond and Naili 2005). In other studies, a poroelastic finite element method has been applied to quantify the fluid pressure behavior in bone tissue (Manfredini et al. 1999; Rémond et al. 2008; Pereira and Shefelbine 2014). Rémond et al. (2008) considered the spatial distribution of bone mechanical properties in finite element simulations to solve the poroelastic problem associated with a hollow cylindrical osteon. In our previous work, we derived an analytical solution containing both transient and steady-state responses for the interstitial fluid pressure in a two-dimensional trabecula when subjected

to cyclic loading (Kameo et al. 2008, 2009). In our analytical study, the trabecula was assumed to be a homogeneous and isotropic material for simplicity, despite the fact that the bone matrix is made of several lamellae.
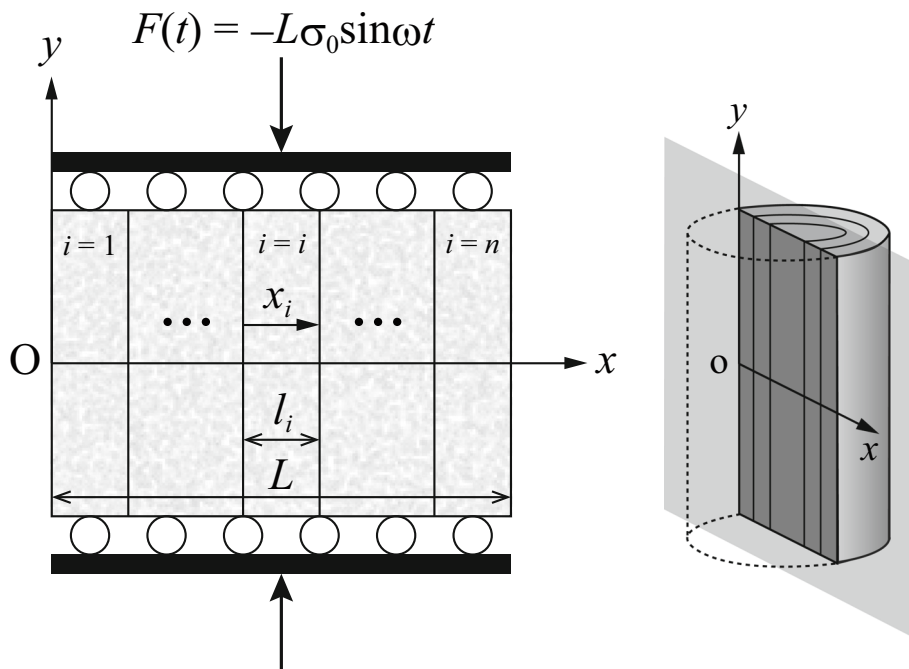
The purpose of the present study is to clarify the effect of the lamellar structure of the bone matrix—i.e., variations in material properties—on the fluid flow stimuli to osteocytes embedded in trabeculae. We used an analytical approach to investigate the response of the interstitial fluid pressure in the lacuno-canalicular porosity within the single trabecula to applied cyclic loading. We focused on variations in permeability because it is a key factor for characterizing the interstitial fluid flow. In our developed model, a single trabecula is idealized as a two-dimensional poroelastic slab composed of multiple layers, where each layer is an isotropic material and has a different value of permeability. We present an analytical solution for the interstitial fluid pressure in the single trabecula as a summation of the transient and steady-state parts by solving the governing equations for the quasi-static poroelasticity. Based on the obtained solution, we demonstrate how variations in permeability influence the pressure and seepage velocity of interstitial fluid, which are associated with the mechanical stimuli to osteocytes.

2 Poroelastic analysis

2.1 Governing equations

We used the linear poroelasticity (Detournay and Cheng 1993; Wang 2000; Coussy 2004) to describe the solid–fluid interaction in a single trabecula under the assumption of small perturbations. In particular, we focused on the quasi-static mechanical behavior because the bone tissue within a living body is usually subjected to low-frequency cyclic loading from activities of daily living.

$$F(t) = -L\sigma_0 \sin\omega t$$

For an isotropic poroelastic material, the total stress tensor σ_{ij} and fluid pressure p satisfy the diffusion equation obtained from the fluid continuity equation:

$$c\nabla^2 \left(\sigma_{kk} + \frac{3}{B}p\right) = \frac{\partial}{\partial t}\left(\sigma_{kk} + \frac{3}{B}p\right), \tag{1}$$

where ∇^2 represents the Laplace operator and the summation convention on repeated indices is adopted. In the above equation, the diffusion coefficient c and Skempton coefficient B are given by

$$c = \frac{k}{\mu}\left[\frac{2GB^2(1-\nu)(1+\nu_u)^2}{9(1-\nu_u)(\nu_u-\nu)}\right] \tag{2}$$

$$B = \frac{1/K - 1/K_s}{\phi/K_f + 1/K - (1+\phi)/K_s}, \tag{3}$$

where G, ν, and K are, respectively, the shear modulus, Poisson's ratio, and the bulk modulus under the drained condition, satisfying $K = 2G(1+\nu)/3(1-2\nu)$. K_s is the solid bulk modulus, K_f is the fluid bulk modulus, ϕ is the porosity, k is the intrinsic permeability, and μ is the dynamic viscosity of the fluid. The undrained Poisson's ratio ν_u can be expressed in the following form:

$$\nu_u = \frac{3\nu + \alpha B(1-2\nu)}{3 - \alpha B(1-2\nu)}, \tag{4}$$

where α is the Biot–Willis coefficient given by

$$\alpha = 1 - \frac{K}{K_s}, \tag{5}$$

Another relationship between the sum of the three normal stresses σ_{kk} and the fluid pressure p can be obtained from the strain compatibility equations:

$$\nabla^2\left[\sigma_{kk} + \frac{2\alpha(1-2\nu)}{(1-\nu)}p\right] = 0. \tag{6}$$

Equations (1)–(6) constitute the set of governing equations to be solved. Seven independent material properties are required for the poroelastic analysis: the permeability k, fluid viscosity μ, drained shear modulus G, drained Poisson's ratio ν, solid bulk modulus K_s, fluid bulk modulus K_f, and porosity ϕ.

2.2 Formulation

For the model of a single lamellar trabecula indicated by the red square in Fig 1, we considered a two-dimensional poroelastic slab consisting of n layers with a width of L in the x-direction and a unit thickness, as shown in Fig. 2. This model represents the longitudinal cross section of an individual cylindrical trabecula, which is a typical trabecula in cancellous bone. To impose uniform external loadings, two rigid and impermeable plates were placed at the top and bottom of this sample in reference to Mandel's problem (Wang 2000; Coussy 2004) and our previous studies (Kameo et al. 2008, 2009). Mandel's problem is a classical problem associated with the compression of a poroelastic slab. In this study, each layer of the poroelastic slab is assumed to be an isotropic material with the same material properties except for the permeability k. The physical quantities associated with the i-th

layer are identified by the subscript i. In addition to the global coordinate system (x, y), a local coordinate x_i is employed by taking the origin at the left side of the i-th layer with a width of l_i, as shown in Fig. 2.

A cyclic uniaxial load along the y-direction $F(t) = -L\sigma_0 \sin \omega t$ is applied to the trabecular model through the plates at time $t = 0$. Considering the problem symmetry, the stress components σ_{ij} and fluid pressure p depend only on x (or x_i) and t. Assuming no shear stresses throughout the poroelastic slab, i.e., $\sigma_{xy} = 0$, and that the slab edges $x = 0, L$ are stress free, the stress equilibrium in the x-direction requires $\sigma_{xx} = 0$. For poroelastic analysis of a single trabecula, the term containing the fluid pressure p in Eq. (6) is negligible because the bone matrix supports much more of the mechanical load than the interstitial fluid (Weinbaum et al. 1994; Kameo et al. 2008). Therefore, under a plane stress condition in the z-direction, i.e., $\sigma_{zz} = 0$, the sum of the three normal stresses σ_{kk} is written as follows:

$$\sigma_{kk} = \sigma_{yy} = -\sigma_0 \sin \omega t. \quad (7)$$

Substituting Eqs. (7) into (1) provides the diffusion equation for the i-th layer:

$$c_i \frac{\partial^2 p_i}{\partial x_i^2} - \frac{\partial p_i}{\partial t} = -\frac{B}{3}\sigma_0 \omega \cos \omega t. \quad (8)$$

When the slab edges at $x = 0, L$ are drained, the initial and boundary conditions for the fluid pressure p can be expressed in the following form:

$$t = 0; \quad p_i = 0 \, (i = 1 \sim n) \quad (9)$$

$$x_1 = 0; \quad p_1 = 0 \quad (10)$$

$$x_i = l_i, x_{i+1} = 0; \quad p_i = p_{i+1},$$
$$-\frac{k_i}{\mu}\frac{\partial p_i}{\partial x_i} = -\frac{k_{i+1}}{\mu}\frac{\partial p_{i+1}}{\partial x_{i+1}} \quad (i = 1 \sim n-1) \quad (11)$$

$$x_n = l_n; \quad p_n = 0, \quad (12)$$

where we consider the continuity of the fluid pressure and fluid flux at the boundaries of the layers.

By introducing the following dimensionless values

$$x_i^* = \frac{x_i}{L}, t^* = \frac{c_0 t}{L^2}, p_i^* = \frac{p_i}{B\sigma_0/3},$$
$$l_i^* = \frac{l_i}{L}, k_i^* = \frac{k_i}{k_0} = \frac{c_i}{c_0}, \Omega = \frac{L^2\omega}{c_0}, \quad (13)$$

with the diffusion equation and the initial and boundary conditions, Eqs. (8)–(12) are rewritten as follows:

$$k_i^* \frac{\partial^2 p_i^*}{\partial x_i^{*2}} - \frac{\partial p_i^*}{\partial t^*} = -\Omega \cos \Omega t^* \quad (14)$$

$$t^* = 0; \quad p_i^* = 0 \quad (i = 1 \sim n) \quad (15)$$

$$x_1^* = 0; \quad p_1^* = 0 \quad (16)$$

$$x_i^* = l_i^*, x_{i+1}^* = 0; \quad p_i^* = p_{i+1}^*,$$
$$k_i^* \frac{\partial p_i^*}{\partial x_i^*} = k_{i+1}^* \frac{\partial p_{i+1}^*}{\partial x_{i+1}^*} \quad (i = 1 \sim n-1) \quad (17)$$

$$x_n^* = l_n^*; p_n^* = 0. \quad (18)$$

In Eq. (13), k_0 and c_0 represent typical values of the permeability and diffusion coefficient that satisfy Eq. (2). Henceforth, we omit the asterisk (*) from the dimensionless values to simplify the notation.

2.3 Solution

We solve the initial and boundary value problems shown in Eqs. (14)–(18) analytically by making use of the Laplace transform technique. By taking the Laplace transform of Eq. (14) with respect to time under the initial condition Eq. (15), the fundamental solution for the fluid pressure can be obtained as follows:

$$\tilde{p}_i = A_i \cosh\sqrt{\frac{s}{k_i}}x_i + B_i \sinh\sqrt{\frac{s}{k_i}}x_i + \frac{\Omega}{s^2 + \Omega^2}, \quad (19)$$

where the tilde ($\tilde{\ }$) signifies the Laplace transform and A_i and B_i are unknown coefficients to be determined from the boundary conditions, Eqs. (16)–(18). By substituting Eq. (19) into Eqs. (16)–(18) after taking the Laplace transform, these equations can be expressed in matrix form:

$$[a_{kl}]\begin{Bmatrix} A_1 \\ B_1 \\ \vdots \\ A_n \\ B_n \end{Bmatrix} = \frac{\Omega}{s^2 + \Omega^2}\begin{Bmatrix} f_1 \\ 0 \\ \vdots \\ 0 \\ f_{2n} \end{Bmatrix} \quad (k, l = 1 \sim 2n), \quad (20)$$

where the nonzero elements among a_{kl} and f_k are given by

$$a_{11} = 1$$
$$a_{2i,2i-1} = \cosh\sqrt{\frac{s}{k_i}}l_i, a_{2i,2i} = \sinh\sqrt{\frac{s}{k_i}}l_i, a_{2i,2i+1} = -1$$
$$a_{2i+1,2i-1} = \sqrt{k_i s}\sinh\sqrt{\frac{s}{k_i}}l_i, a_{2i+1,2i} = \sqrt{k_i s}\cosh\sqrt{\frac{s}{k_i}}l_i,$$
$$a_{2i+1,2i+1} = -\sqrt{k_{i+1}s} \, (i = 1 \sim n-1)$$
$$a_{2n,2n-1} = \cosh\sqrt{\frac{s}{k_n}}l_n, a_{2n,2n} = \sinh\sqrt{\frac{s}{k_n}}l_n$$
$$f_1 = -1, f_{2n} = -1. \quad (21)$$

By applying Cramer's rule to the system of equations in Eq. (20), the fluid pressure solution in the Laplace transformed domain is obtained as follows:

$$\tilde{p}_i = \frac{\Omega}{\Delta \left(s^2 + \Omega^2\right)} \left(\bar{A}_i \cosh \sqrt{\frac{s}{k_i}} x_i + \bar{B}_i \sinh \sqrt{\frac{s}{k_i}} x_i + \Delta\right),$$

$$(22)$$

where Δ is the determinant of the matrix $[a_{kl}]$ and $\bar{A}_i$ and $\bar{B}_i$ are the determinants of the matrix formed by replacing the $(2i-1)$-th and $2i$-th columns, respectively, of the matrix $[a_{kl}]$ by the column vector $\{f_k\}$. The inverse Laplace transform of Eq. (22) from using the residue theorem eventually provides the solution to the fluid pressure in the form of the summation of the steady-state solution p_i^{steady} and transient solution p_i^{trans}:

$$p_i = p_i^{\text{steady}} + p_i^{\text{trans}}, \qquad (23)$$

where the first term is the sum of the residues corresponding to the simple poles $s = \pm i\Omega$ and the second term is the sum of the residues corresponding to the roots of $\Delta = 0$. The steady-state solution p_i^{steady} can be derived as follows:

$$p_i^{\text{steady}}$$

$$= \text{Im} \left[\frac{\bar{A}_i|_{s=i\Omega} \cosh \sqrt{\frac{i\Omega}{k_i}} x_i + \bar{B}_i|_{s=i\Omega} \sinh \sqrt{\frac{i\Omega}{k_i}} x_i + \Delta|_{s=i\Omega}}{\Delta|_{s=i\Omega}} e^{i\Omega t} \right],$$

$$(24)$$

where Im gives the imaginary part of the complex number.

To obtain the transient solution p_i^{trans}, it is convenient to put $s = -\lambda^2 (\lambda > 0)$. By using this notation, Eqs. (19)–(22) are rewritten in the following form:

$$\tilde{p}_i = A_i' \cos \frac{\lambda}{\sqrt{k_i}} x_i + B_i' \sin \frac{\lambda}{\sqrt{k_i}} x_i + \frac{\Omega}{\lambda^4 + \Omega^2} \qquad (25)$$

$$[e_{kl}] \begin{Bmatrix} A_1' \\ B_1' \\ \vdots \\ A_n' \\ B_n' \end{Bmatrix} = \frac{\Omega}{\lambda^4 + \Omega^2} \begin{Bmatrix} f_1 \\ 0 \\ \vdots \\ 0 \\ f_{2n} \end{Bmatrix} \quad (k, l = 1 \sim 2n) \qquad (26)$$

$$e_{11} = 1$$

$$e_{2i,2i-1} = \cos \frac{\lambda}{\sqrt{k_i}} l_i, \ e_{2i,2i} = \sin \frac{\lambda}{\sqrt{k_i}} l_i, \ e_{2i,2i+1} = -1$$

$$e_{2i+1,2i-1} = -\lambda \sqrt{k_i} \sin \frac{\lambda}{\sqrt{k_i}} l_i, \ e_{2i+1,2i} = \lambda \sqrt{k_i} \cos \frac{\lambda}{\sqrt{k_i}} l_i,$$

$$e_{2i+1,2i+1} = -\lambda \sqrt{k_{i+1}} \ (i = 1 \sim n-1)$$

$$e_{2n,2n-1} = \cos \frac{\lambda}{\sqrt{k_n}} l_n, \ e_{2n,2n} = \sin \frac{\lambda}{\sqrt{k_n}} l_n$$

$$f_1 = -1, \ f_{2n} = -1 \qquad (27)$$

$$\tilde{p}_i = \frac{\Omega}{D\left(\lambda^4 + \Omega^2\right)} \left(\bar{A}_i' \cos \frac{\lambda}{\sqrt{k_i}} x_i + \bar{B}_i' \sin \frac{\lambda}{\sqrt{k_i}} x_i + D\right), \quad (28)$$

where D is the determinant of the matrix $[e_{kl}]$ and $\bar{A}_i'$ and $\bar{B}_i'$ are the determinants of the matrix formed by replacing the $(2i-1)$-th and $2i$-th columns, respectively, of the matrix $[e_{kl}]$ by the column vector $\{f_k\}$. By taking the inverse Laplace transform of Eq. (28) with the help of the residue theorem, the transient solution of fluid pressure p_i^{trans} can be derived as the sum of the residues corresponding to the roots of $D = 0$ as follows:

$$p_i^{\text{trans}} = \sum_{j=1}^{\infty} \frac{-2\lambda_j e^{-\lambda_j^2 t}}{\frac{dD}{d\lambda}\big|_{\lambda=\lambda_j}} \left[\bar{A}_i'\big|_{\lambda=\lambda_j} \cos \frac{\lambda_j}{\sqrt{k_i}} x_i + \bar{B}_i'\big|_{\lambda=\lambda_j} \sin \frac{\lambda_j}{\sqrt{k_i}} x_i \right] \frac{\Omega}{\lambda_j^4 + \Omega^2}, \qquad (29)$$

where λ_j is the j-th positive roots of $D(\lambda) = 0$. For the calculation of the derivative in Eq. (29), the following relation can be used:

$$\frac{dD}{d\lambda}\bigg|_{\lambda=\lambda_j} = \sum_{m=1}^{2n} M_m, \qquad (30)$$

where M_m is the determinant of the matrix formed by replacing the m-th column of the matrix $[e_{kl}]$ by the derivative of the same column with respect to λ.

2.4 Single trabecular model

Table 1 lists the material properties used in the poroelastic modeling of a single trabecula (Smit et al. 2002; Beno et al. 2006). Among these material constants, the intrinsic permeability k_0 and porosity ϕ are especially important factors that influence the interstitial fluid pressure and seepage velocity. Because the values of these two factors are more sensitive to changes in lacuno-canalicular morphology compared with those of the other five constants, it is essential to set k_0 and ϕ appropriately in order to quantify the fluid flow stimuli for osteocytes. While there is generally a positive correlation between permeability and porosity (Kameo et al. 2010), we considered variations in only permeability and ignored variations in porosity for simplicity.

Table 1 Material properties of trabecula as poroelastic material (Smit et al. 2002; Beno et al. 2006)

Symbol (unit)	Description	Value
k_0 (m^2)	Intrinsic permeability	1.1×10^{-21}
μ (Pa s)	Fluid viscosity	1.0×10^{-3}
G (GPa)	Shear modulus	5.94
v	Drained Poisson's ratio	0.325
K_s (GPa)	Solid bulk modulus	17.66
K_f (GPa)	Fluid bulk modulus	2.3
ϕ	Porosity	0.05

Permeability was estimated by the method of Beno et al. (2006)
The other constants were taken from Smit et al. (2002)

Table 2 Settings of trabecular permeability for poroelastic analysis

	Normalized permeability					
	k_1^*	k_2^*	k_3^*	k_4^*	k_5^*	k_6^*
Case 1	0.5	0.7	0.9	1.1	1.3	1.5
Case 2	0.5	1.0	1.5	1.5	1.0	0.5
Case 3	1.5	1.0	0.5	0.5	1.0	1.5

By using seven independent material properties in Table 1, the poroelastic constants defined in Sect. 2.1 (i.e., the Biot–Willis coefficient α [Eq. (5)], undrained Poisson's ratio ν_u [Eq. (4)], Skempton coefficient B [Eq. (3)], and typical value of the diffusion coefficient c_0 [Eq. (2)]) are, respectively, derived as follows: $\alpha = 0.15$, $\nu_u = 0.33$, $B = 0.35$, and $c_0 = 3.9 \times 10^{-8} \, \mathrm{m^2/s}$. Considering that an individual trabecula in vivo has a typical width of $L = 200 \, \mu\mathrm{m}$ and is subjected to 1–20 Hz cyclic loading (Weinbaum et al. 1994), the range of the dimensionless frequency Ω defined in Eq. (13) is estimated to be between 6.5 and 130. Therefore, we set two different values of Ω ($\Omega = 10$ and 100) to investigate the role of the loading frequency.

The total number of layers that constitute a single trabecula was selected as $n = 6$, which is within the physiological range. Each layer was assumed to have the same width. The spatial variations in trabecular permeability are difficult to determine because the size of the lacuno-canalicular porosity can vary according to osteocytic remodeling of the perilacunar and pericanalicular matrix (Qing and Bonewald 2009). Therefore, in order to investigate their effect on the behavior of interstitial fluid, we considered three cases, all of which have the same average permeability. Case 1 deals with a single trabecula in which the permeability is linearly distributed from the first layer to the sixth layer and has the following settings: $k_1 = 0.5$, $k_2 = 0.7$, $k_3 = 0.9$, $k_4 = 1.1$, $k_5 = 1.3$, and $k_6 = 1.5$. In the equilibrium state of bone remodeling, an individual cylindrical trabecula may have an axisymmetrical lamellar structure. In order to account for such conditions, the other two cases consider the trabeculae with a symmetrical distribution of permeability about the central axis $x = L/2$: in Case 2, $k_1 = 0.5$, $k_2 = 1.0$, $k_3 = 1.5$, $k_4 = 1.5$, $k_5 = 1.0$, and $k_6 = 0.5$; in Case 3, $k_1 = 1.5$, $k_2 = 1.0$, $k_3 = 0.5$, $k_4 = 0.5$, $k_5 = 1.0$, and $k_6 = 1.5$. In Case 2, the interstitial fluid around the center of trabecula can flow through more easily than the fluid close to the trabecular surfaces, while Case 3 represents the reverse condition. Table 2 summarizes the settings of the trabecular permeability in the above three cases.

3 Results

3.1 Fluid pressure

The fluid pressure in a single trabecula under cyclic loading was calculated according to Eqs. (24) and (29). Figure 3

shows the fluid pressure distributions along the x-direction in Case 1, where the permeability was linearly distributed (see Table 2). Figure 3a, b corresponds to the steady-state responses for the dimensionless frequencies $\Omega = 10$ and 100, respectively, plotted for eight equal-length phase points in a period. Figure 3c, d corresponds to the transient responses for $\Omega = 10$ and 100, respectively, plotted at $t^* = 0, 0.01, 0.1$, and 1. All of the figures exhibit asymmetrical fluid pressure distributions about the central axis $x^* = 0.5$ owing to the spatial gradient of permeability. As shown in Fig. 3a, b, increasing the dimensionless frequency Ω caused the fluid pressure profile in steady state to transform from a parabolic shape to a trapezoidal shape. Thus, the fluid pressure gradient around the trabecular surfaces built up because of the increase in Ω. The fluid pressure gradient at the edge $x^* = 0$, where the value of permeability was smaller, was larger than that at the other edge $x^* = 1$ when the loading frequency was constant.

As shown in Fig. 3c, d, the transient stage was observed after cyclic loading was applied, and it decayed within the time $t^* = 1$. The magnitude of the transient response was related to the fluid pressure profile in steady state at the phase point 0 because the sum of the transient and steady-state fluid pressures at $t^* = 0$ must be null by the initial conditions, Eqs. (9), (15). Figure 3c, d indicates that the effect of the transient response is more important at low loading frequencies than at high loading frequencies.

Figures 4 and 5 show the fluid pressure distributions in the steady state along the x-direction in Cases 2 and 3, respectively, where the permeability was symmetrically distributed (see Table 2). In these figures, part (a) corresponds to the result for the dimensionless frequency $\Omega = 10$ and part (b) corresponds to the result for $\Omega = 100$. As shown in Figs. 4a and 5a, the maximum values of both the fluid pressure and its spatial gradient for $\Omega = 10$ were larger in Case 2, where the value of permeability close to the trabecular surfaces was less than that around the center of trabecula. On the other hand, for the loading frequency $\Omega = 100$, the peak values of the fluid pressure in Cases 2 and 3 were almost the same, whereas the fluid pressure gradient around the trabecular surfaces was larger in Case 2 than in Case 3, as shown in Figs. 4b and 5b.

3.2 Seepage velocity

The seepage velocity in poroelastic materials is one of the mechanical properties that quantifies the fluid flow at the macroscopic scale. In the context of bone poroelasticity, the seepage velocity represents the average velocity of interstitial fluid in a lacuno-canalicular porosity and is closely associated with the mechanical stimuli to osteocytes during the bone remodeling process. According to Darcy's law, the x
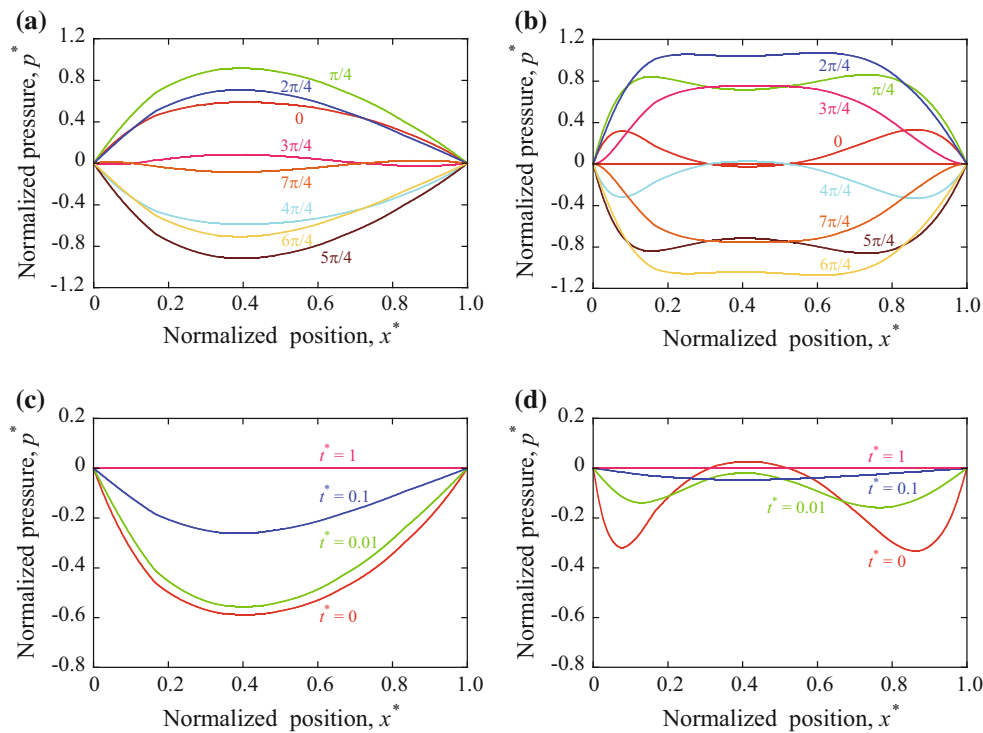
(a)

(b)

(c)

(d)

Fig. 3 Fluid pressure distribution along x-direction in Case 1 ($k_1^* = 0.5, k_2^* = 0.7, k_3^* = 0.9, k_4^* = 1.1, k_5^* = 1.3, k_6^* = 1.5$). Steady-state response: **a** $\Omega = 10$, **b** $\Omega = 100$. Transient response: **c** $\Omega = 10$, **d** $\Omega = 100$
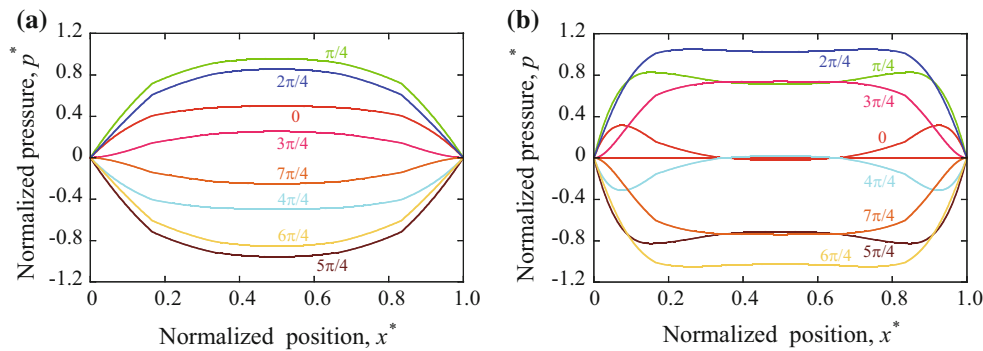
(a)

(b)

Fig. 4 Fluid pressure distribution in steady state along x-direction in Case 2 ($k_1^* = 0.5, k_2^* = 1.0, k_3^* = 1.5, k_4^* = 1.5, k_5^* = 1.0, k_6^* = 0.5$): **a** $\Omega = 10$ and **b** $\Omega = 100$
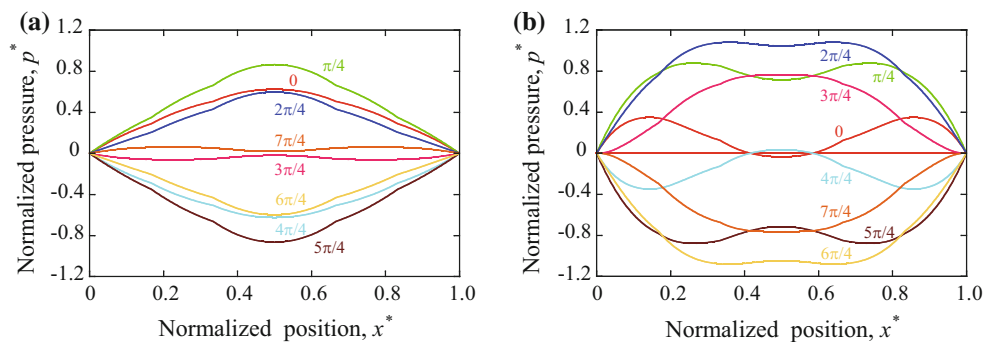
(a)

(b)

Fig. 5 Fluid pressure distribution in steady state along x-direction in Case 3 ($k_1^* = 1.5, k_2^* = 1.0, k_3^* = 0.5, k_4^* = 0.5, k_5^* = 1.0, k_6^* = 1.5$): **a** $\Omega = 10$ and **b** $\Omega = 100$
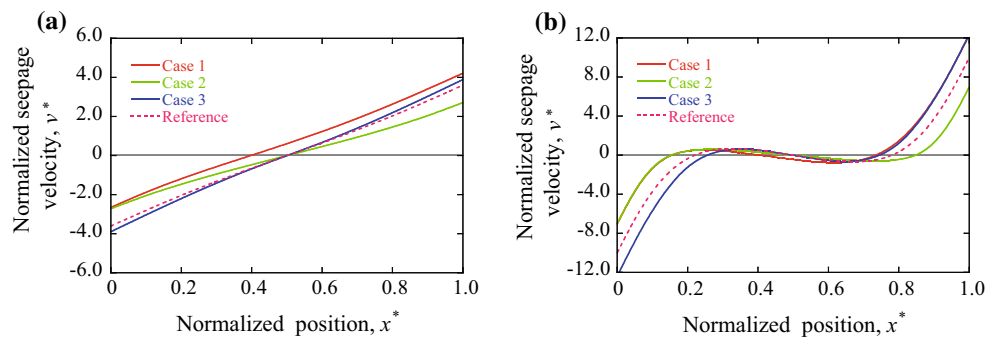
Fig. 6 Seepage velocity distribution in steady state along x-direction for **a** $\Omega = 10$ and **b** $\Omega = 100$: Case 1 ($k_1^* = 0.5, k_2^* = 0.7, k_3^* = 0.9, k_4^* = 1.1, k_5^* = 1.3, k_6^* = 1.5$); Case 2 ($k_1^* = 0.5, k_2^* = 1.0, k_3^* = 1.5, k_4^* = 1.5, k_5^* = 1.0, k_6^* = 0.5$); Case 3 ($k_1^* = 1.5, k_2^* = 1.0, k_3^* = 0.5, k_4^* = 0.5, k_5^* = 1.0, k_6^* = 1.5$) and constant permeability $k_i^* = 1.0$ ($i = 1 \sim 6$) as reference

component of the seepage velocity for the i-th layer v_i is given by

$$v_i = -\frac{1}{\phi}\frac{k_i}{\mu}\frac{\partial p_i}{\partial x_i}. \tag{31}$$

If we introduce the following dimensionless seepage velocity

$$v_i^* = \frac{v_i}{B\sigma_0 k_0/3\mu L\phi}, \tag{32}$$

this quantity can be expressed as

$$v_i^* = -k_i^*\frac{\partial p_i^*}{\partial x_i^*}. \tag{33}$$

By substituting Eqs. (23) into (33) with the help of Eqs. (24) and (29), the solution for the dimensionless seepage velocity can be obtained. In this study, we focused only on the seepage velocity behavior in the steady state.

Figure 6 shows the seepage velocity distributions in the steady state along the x-direction in Cases 1–3 at the fluid pressure peak. Figure 6a corresponds to the result for the dimensionless frequency $\Omega = 10$, and Fig 6b corresponds to the result for $\Omega = 100$. In both parts of the figure, the profile of the seepage velocity in the single trabecula with constant permeability, i.e., $k_i^* = 1.0$ ($i = 1 \sim 6$), is presented as a reference result. As shown in Fig. 6a, the seepage velocity for $\Omega = 10$ was almost linearly distributed across the trabecula, and its maximum value was observed at the edge $x^* = 1$ in Case 1. When the loading frequency was $\Omega = 100$, as shown in Fig. 6b, the seepage velocity around the center of trabecula was negligible for all permeability values. The distribution curves in Cases 1 and 2 overlapped near the edge $x^* = 0$, and the curves in Cases 1 and 3 also overlapped in the neighborhood of the other edge $x^* = 1$. The maximum seepage velocity was larger in Case 3 than in Case 2, in contrast to the results for the fluid pressure gradient presented in the previous section.

4 Discussion

We developed an analytical solution for the interstitial fluid pressure in the lacuno-canalicular porosity within a single trabecula modeled as a two-dimensional multilayered poroelastic material subjected to cyclic loading, in which each layer has a different value of permeability. Based on the obtained transient and steady-state solutions, we investigated the effect of variations in permeability on the behavior of interstitial fluid. Poroelastic analysis showed that a heterogeneous distribution of permeability produces remarkable variations in the fluid pressure and seepage velocity in the cross section of the individual trabecula.

The trabecular permeability depends on both the dimensions of the lacuno-canalicular porosity and its microstructure, such as the tortuosity, bifurcation, and the density of the pericellular matrix (Beno et al. 2006; Kameo et al. 2010). Measuring the exact value of the intrinsic permeability is extremely difficult because the lacuno-canalicular porosity has a complex three-dimensional structure with a diameter of only several hundred nanometers. Despite extensive research to determine the bone permeability, the estimated range based on theoretical and experimental approaches is quite broad: from 10^{-26} to 10^{-18} m^2 (Zhang et al. 1998; Smit et al. 2002; Beno et al. 2006; Oyen 2008; Gailani et al. 2009; Kameo et al. 2010). In our study, we set the approximate median value of $k_0 = 1.1 \times 10^{-21}$ m^2 as the representative permeability, which was determined based on the method proposed by Beno et al. (2006). The magnitude of the trabecular permeability k_0 is reflected in the dimensionless frequency Ω, as shown in Eqs. (2) and (13). As the order of magnitude of permeability increases or the dimensionless frequency Ω decreases, the peak fluid pressure decreases due to rapid leakage from the trabecular surfaces. On the other hand, as the order of permeability decreases or Ω increases, the fluid pressure response approaches undrained behavior; this leads to no flow in the whole region except for the neighborhood of the trabecular surfaces.

Computer simulations have been utilized in order to understand how the bone permeability affects mechanical stimuli at the cellular level (Manfredini et al. 1999; Rémond et al. 2008; Pereira and Shefelbine 2014). Rémond et al. (2008) investigated the effect of spatial gradients of the permeability on the interstitial fluid flow using poroelastic finite element analysis of an osteon in cortical bone. They reported that permeability gradients do not cause a notable variation of the fluid velocity distribution, in contrast to our results shown in Fig. 6. Although this has interesting implications for cellular mechanosensing, such behavior of the interstitial fluid can only be observed when the permeability is sufficiently large ($\sim 10^{-18}$ m^2), i.e., under nearly drained conditions. As shown in Fig. 6, the seepage velocity is generally influenced by the permeability distribution, and its sensitivity depends on the rate of loading relative to the permeability, which was defined as the dimensionless frequency Ω in this study.

The seepage velocity of the interstitial fluid can be considered as a characteristic of the mechanical stimuli to osteocytes embedded in trabeculae. This quantity is related to the fluid pressure gradient, which is a driving force of the fluid flow according to Eq. (31). As noted in the previous section, the distribution of the seepage velocity in the single trabecula does not coincide with that of the fluid pressure gradient because the permeability is not constant. The applied loading frequency is one of the most important factors that affect the behavior of the interstitial fluid. Figure 6 shows that as the dimensionless frequency Ω increases, the seepage velocity and thus the mechanical stimuli to osteocytes close to the trabecular surfaces increases, while the flow around the center of trabecula decreases. Considering the in vivo experimental results, which showed that a more significant bone ingrowth was induced at higher loading rates (Goldstein et al. 1991), the results obtained in the current analytical study imply that osteocytes buried in the neighborhood of the trabecular surfaces primarily work as mechanosensory cells during the bone remodeling process.

Comparing the seepage velocity near the surfaces between three cases of trabeculae in Fig. 6 indicates that the maximum seepage velocity and thus the maximum fluid flow stimuli to osteocytes are mostly governed by the value of permeability in the neighborhood of the trabecular surfaces if there is no difference in the average permeability in a single trabecula. In particular, large mechanical stimuli for osteocytes could be found around trabecular surfaces with relatively large permeability. According to the Frost's mechanostat theory (Frost 1987, 2003), the single trabecula in Case 3, i.e., the trabecula in which the permeability close to the trabecular surfaces is relatively large, has a higher potential for bone formation via trabecular surface remodeling. These results suggest that the bone resorption and formation on the trabecular surface can be influenced by the changes in the dimension and microstructure of the neighboring lacuno-canalicular porosity as well as the changes in the trabecular volume or external loads. Even as the capability of osteocytes to remove old mineral and to deposit new mineral is still under discussion (Qing and Bonewald 2009), it is possible that osteocyte mechanotransduction via interstitial fluid flow and the subsequent trabecular bone adaptation to the mechanical loads is regulated to some extent by osteocytic remodeling of the lacuno-canalicular porosity. Indeed, significant differences in the structural architecture of the osteocyte networks in the parietal bone (flat bone) and tibia (long bone) have been previously noted (Himeno-Ando et al. 2012); and this experimental fact suggests a strong correlation between the architecture of the lacuno-canalicular porosity and the physiological loading patterns to these bones.

In the present analysis, we modeled a single trabecula as a two-dimensional poroelastic slab with isotropic material properties, for the sake of simplicity. However, an individual trabecula in vivo has a cylindrical morphology, and the mechanical behavior can be regarded as transversely isotropic (Turner et al. 1999; Rémond and Naili 2005; Rémond et al. 2008) owing to the component mineral crystals and collagen fibers. Furthermore, we assumed only that permeability is not constant among the poroelastic material properties listed in Table 1, even though the permeability k is closely related to the porosity ϕ (Kameo et al. 2010). Nevertheless, this poroelastic analysis provides fundamental knowledge on interstitial fluid behavior under physiological cyclic loading when permeability is spatially distributed in a single trabecula. By setting the appropriate distribution of permeability in an individual trabecula based on experimental findings, the current theoretical analysis would help understand the relationship between the macroscopic loads applied to the trabecula and the resulting microscopic mechanical environment of osteocytes within the trabecula, which is in turn associated directly with bone remodeling.

References

Beno T, Yoon YJ, Cowin SC, Fritton SP (2006) Estimation of bone permeability using accurate microstructural measurements. J Biomech 39:2378–2387

Biot MA (1941) General theory of three-dimensional consolidation. J Appl Phys 12:155–164

Biot MA (1955) Theory of elasticity and consolidation for a porous anisotropic solid. J Appl Phys 26:182–185

Bonewald LF (2011) The amazing osteocyte. J Bone Miner Res 26:229–238

Burger EH, Klein-Nulend J (1999) Mechanotransduction in bone-role of the lacuno-canalicular network. FASEB J 13:S101–S112

Coussy O (2004) Poromechanics. Wiley, West Sussex

Cowin SC (1999) Bone poroelasticity. J Biomech 32:217–238

Cowin SC, Moss-Salentijn L, Moss ML (1991) Candidates for the mechanosensory system in bone. J Biomech Eng 113:191–197

Detournay E, Cheng AH-D (1993) Fundamentals of poroelasticity. Comprehensive rock engineering: principles, practice and projects. In: Fairhurst C (ed) Analysis and design method, vol II. Pergamon Press, Oxford, pp 113–171 (Chapter 5)

Frost HM (1987) Bone "mass" and the "mechanostat": a proposal. Anat Rec 219:1–9

Frost HM (2003) Bone's mechanostat: a 2003 update. Anat Rec A Discov Mol Cell Evol Biol 275:1081–1101

Gailani G, Benalla M, Mahamud R, Cowin SC, Cardoso L (2009) Experimental determination of the permeability in the lacunar-canalicular porosity of bone. J Biomech Eng 131:101007

Goldstein SA, Matthews LS, Kuhn JL, Hollister SJ (1991) Trabecular bone remodeling: an experimental model. J Biomech 24:135–150

Himeno-Ando A, Izumi Y, Yamaguchi A, Iimura T (2012) Structural differences in the osteocyte network between the calvaria and long bone revealed by three-dimensional fluorescence morphometry, possibly reflecting distinct mechano-adaptations and sensitivities. Biochem Biophys Res Commun 417:765–770

Kameo Y, Adachi T, Hojo M (2008) Transient response of fluid pressure in a poroelastic material under uniaxial cyclic loading. J Mech Phys Solids 56:1794–1805

Kameo Y, Adachi T, Hojo M (2009) Fluid pressure response in poroelastic materials subjected to cyclic loading. J Mech Phys Solids 57:1815–1827

Kameo Y, Adachi T, Hojo M (2010) Estimation of bone permeability considering the morphology of lacuno-canalicular porosity. J Mech Behav Biomed Mater 3:240–248

Kameo Y, Adachi T (2014) Interstitial fluid flow in canaliculi as a mechanical stimulus for cancellous bone remodeling: in silico validation. Biomech Model Mechanobiol 13:851–860

Manfredini P, Cocchetti G, Maier G, Redaelli A, Montevecchi FM (1999) Poroelastic finite element analysis of a bone specimen under cyclic loading. J Biomech 32:135–144

Martin RB, Burr DB, Sharley NA (1998) Skeletal tissue mechanics. Springer, New York

Nakashima T, Hayashi M, Fukunaga T, Kurata K, Oh-hora M, Feng JQ, Bonewald LF, Kodama T, Wutz A, Wagner EF, Penninger JM, Takayanagi H (2011) Evidence for osteocyte regulation of bone homeostasis through RANKL expression. Nat Med 17:231–1234

Oyen ML (2008) Poroelastic nanoindentation responses of hydrated bone. J Mater Res 23:1307–1314

Parfitt AM (1994) Osteonal and hemi-osteonal remodeling: the spatial and temporal framework for signal traffic in adult human bone. J Cell Biochem 55:273–286

Pereira AF, Shefelbine SJ (2014) The influence of load repetition in bone mechanotransduction using poroelastic finite-element models: the impact of permeability. Biomech Model Mechanobiol 13:215–225

Price C, Zhou X, Li W, Wang L (2011) Real-time measurement of solute transport within the lacunar-canalicular system of mechanically loaded bone: direct evidence for load-induced fluid flow. J Bone Miner Res 26:277–285

Qing H, Bonewald LF (2009) Osteocyte remodeling of the perilacunar and pericanalicular matrix. Int J Oral Sci 1:59–65

Rémond A, Naili S (2005) Transverse isotropic poroelastic osteon model under cyclic loading. Mech Res Commun 32:645–651

Rémond A, Naili S, Lemaire T (2008) Interstitial fluid flow in the osteon with spatial gradients of mechanical properties: a finite element study. Biomech Model Mechanobiol 7:487–495

Smit TH, Huyghe JM, Cowin SC (2002) Estimation of the poroelastic parameters of cortical bone. J Biomech 35:829–835

Sugawara Y, Kamioka H, Honjo T, Tezuka K, Takano-Yamamoto T (2005) Three-dimensional reconstruction of chick calvarial osteocytes and their cell processes using confocal microscopy. Bone 36:877–883

Tatsumi S, Ishii K, Amizuka N, Li MQ, Kobayashi T, Kohno K, Ito M, Takeshita S, Ikeda K (2007) Targeted ablation of osteocytes induces osteoporosis with defective mechanotransduction. Cell Metab 5:464–475

Turner VH, Rho J, Takano Y, Tsui TY, Pharr GM (1999) The elastic properties of trabecular and cortical bone tissues are similar: results from two microscopic measurement techniques. J Biomech 32:437–441

Wang HF (2000) Theory of Linear Poroelasticity with applications to geomechanics and hydrogeology. Princeton University Press, Princeton

Weinbaum S, Cowin SC, Zeng Y (1994) A model for the excitation of osteocytes by mechanical loading-induced bone fluid shear stresses. J Biomech 27:339–360

Zeng Y, Cowin SC, Weinbaum S (1994) A fiber matrix model for fluid flow and streaming potentials in the canaliculi of an osteon. Ann Biomed Eng 22:280–292

Zhang D, Cowin SC (1994) Oscillatory bending of a poroelastic beam. J Mech Phys Solids 42:1575–1599

Zhang D, Weinbaum S, Cowin SC (1998) Estimates of the peak pressures in bone pore water. J Biomech Eng 120:697–703